remote sensing

MDPI

Article

High-Resolution Sea Surface Temperature Retrieval from Landsat 8 OLI/TIRS Data at Coastal Regions

Jae-Cheol Jang [1] and Kyung-Ae Park [2,*]

[1] Department of Science Education, Seoul National University, Seoul 08826, Korea; jaecheol00@snu.ac.kr
[2] Department of Earth Science Education/Research Institute of Oceanography, Seoul National University, Seoul 08826, Korea
* Correspondence: kapark@snu.ac.kr; Tel.: +82-2-880-7780

Received: 25 October 2019; Accepted: 15 November 2019; Published: 18 November 2019

Abstract: High-resolution sea surface temperature (SST) images are essential to study the highly variable small-scale oceanic phenomena in a coastal region. Most previous SST algorithms are focused on the low or medium resolution SST from the near polar orbiting or geostationary satellites. The Landsat 8 Operational Land Imager and Thermal Infrared Sensor (OLI/TIRS) makes it possible to obtain high-resolution SST images of coastal regions. This study performed a matchup procedure between 276 Landsat 8 images and in-situ temperature measurements of buoys off the coast of the Korean Peninsula from April 2013 to August 2017. Using the matchup database, we investigated SST errors for each formulation of the Multi-Channel SST (MCSST) and the Non-Linear SST (NLSST) by considering the satellite zenith angle (SZA) and the first-guess SST. The retrieved SST equations showed a root-mean-square error (RMSE) from 0.59 to 0.72 °C. The smallest errors were found for the NLSST equation that considers the SZA and uses the first-guess SST, compared with the MCSST equations. The SST errors showed characteristic dependences on the atmospheric water vapor, the SZA, and the wind speed. In spite of the narrow swath width of the Landsat 8, the effect of the SZA on the errors was estimated to be significant and considerable for all the formations. Although the coefficients were calculated in the coastal regions around the Korean Peninsula, these coefficients are expected to be feasible for SST retrieval applied to any other parts of the global ocean. This study also addressed the need for high-resolution coastal SST, by emphasizing the usefulness of the high-resolution Landsat 8 OLI/TIRS data for monitoring the small-scale oceanic phenomena in coastal regions.

Keywords: sea surface temperature; Landsat 8 OLI/TIRS; SST coefficients; satellite zenith angle

1. Introduction

Sea surface temperature (SST) plays an important role in monitoring and understanding a variety of oceanic and atmospheric phenomena in space and time. In addition to the high-quality in-situ temperature measurements, including the data obtained by surface drifters, moored buoys, or ship of opportunity measurements, accurate satellite-observed SSTs are of importance for diverse purposes and have been operationally used with satisfaction [1,2]. The satellite-observed SST databases have been produced and extensively utilized for investigating SST fronts [3,4], mesoscale eddy dynamics [5], ocean surface current [6], air-sea interaction [7], and their effects on climate change [8]. They are also used as input data for atmospheric and oceanic circulation models as well as for data assimilation purposes [9,10].

Using brightness temperatures (BT) of infrared sensors on satellites, the SSTs have been retrieved based on multi-channel algorithms since the 1970s [11,12]. Multi-Channel SST (MCSST) [13–16] and Non-Linear SST (NLSST) [17–20] have been the most commonly used infrared-based SST retrieval

algorithms as operational algorithms for the National Oceanic and Atmospheric Administration (NOAA) and Advanced Very High-Resolution Radiometer (AVHRR) data in the past decades. Most of the near-polar orbiting satellites have shown accuracy of a root-mean-square error (RMSE) of less than 1 K for the global ocean as well as the regional seas [21–26]. Most of these studies have focused on the satellite imagery with medium or low spatial resolution of a few kilometers, such as 1 km in the case of NOAA/AVHRR or 4 km in the case of geostationary satellites [27–29]. However, in the onshore or offshore regions near the coasts, satellite SST images with a finer spatial resolution, equal to or below 100 m, are required because of the highly complicated coastal lines and complex coastal morphology, the presence of numerous islands, estuaries, small-scale SST gradients that affect fisheries and air-sea fluxes, as well as other oceanic features in coastal regions.

Geostationary satellite-based SSTs have high capability to observe short-term variations of oceanic features with high temporal resolution. Near-polar orbiting satellites can provide detailed SST distributions containing relatively smaller spatial scale of oceanic phenomena compared with the geostationary satellite images. However, much higher spatial resolution is required to monitor the small-scale features in the coastal regions and to study the environment and small-scale features of estuaries and coastal regions [30–32]. Based on the power spectral density of SSTs, it has been known that an abundance of coastal processes are related to submesoscale features with lateral scales of O(1) km, which is smaller than the mesoscale features with spatial scales from 10 to 100 km [33,34]. Some of the previous investigations have conducted studies on how to blend sub-kilometer SST images and in-situ measurements for coastal environment analysis [35–39]. Although the merged SST field produced by synthesizing in-situ and remote sensing data showed good performance in the ocean, careful evaluation is needed due to the uncertainty in coastal regions [40–42].

The Landsat mission is one of the satellites operated by the Earth Observation Program of the National Aeronautics and Space Administration (NASA) for coastal regions; it was launched by developing and improving the sensors sequentially from Landsat 1 in 1972 to Landsat 8 in 2013. Currently, the Landsat 7 Enhanced Thematic Mapper Plus (ETM+) and the Landsat 8 Operational Land Imager and Thermal Infrared Sensor (OLI/TIRS) are in operation [43]. In particular, one of the largest contributing factors of the Landsat 8 OLI/TIRS, compared with the previous Landsat satellites is that the Landsat 8 contains thermal infrared channels centered at 11 and 12 μm [44]. Prior to Landsat 8, the previous Landsat satellites utilized an algorithm based on a mono-window method using single channel data for SST retrieval [45–47]. The Landsat 8 OLI/TIRS made it possible to apply a split window method using a multi-channel for the estimation of SSTs [48–55]. However, all of these studies have used a small number of Landsat 8 images and matchup points of less than 20. None of the previous studies have used several hundreds of Landsat 8 images and addressed an appropriate formulation of the SST equations including potential errors. Therefore, it is necessary to collect more matchups by extending the total period of the collocation procedure, to derive the coefficients of the SST algorithms using considerable in-situ measurements.

In response to this necessity, the main purposes of this study are: (1) to collect in-situ temperature measurements from buoy stations, (2) to apply quality control (QC) processes to the in-situ measurements, (3) to produce a matchup database between the Landsat 8 data and the in-situ data by applying a series of cloud removal methods, (4) to retrieve the SST coefficients for each SST algorithm based on the split window method, (5) to assess the accuracy of the estimated SSTs, (6) to understand the characteristics of SST errors by presenting the most appropriate formulation of the SST equation, and (7) to discuss the errors by conducting a validation procedure.

2. Data

2.1. Study Area

The Korean Peninsula is located at the marginal region of the Northwestern Pacific Ocean and is influenced by the warm and cold currents that result in various marine environmental characteristics

and their seasonality (Figure 1a). The coastal regions around the peninsula, connected with the Yellow Sea, the East Sea/Japan Sea (EJS), and the East China Sea, are very shallow with a mean depth of only 44 m and a maximum depth of 152 m. The western coastal regions have strong tidal currents in the Yellow Sea, however, the bathymetry of the coastal regions of the EJS is comparatively deep, amounting to a few thousand meters (Figure 1b). For the SST retrieval procedure, a wide range of SST variations is important for the stable use of the SST retrieval equations. The seasonal variations of SSTs are dominant with a wide range of SSTs between winter and summer as shown in the Operational Sea Surface Temperature and Sea Ice Analysis (OSTIA) SST climatology for the period of 2002 to 2015 (Figure 1c,d). In addition to the range of SST variations, the accuracy of infrared channel-based SST is extensively affected by changes in the marine environment, such as bathymetry, land mass, tidal flat, tidal current, river discharge, and so on [56,57]. Therefore, this study region is suitable for the calculation of infrared SST coefficients and validation of the equations because of these diverse marine and atmospheric characteristics. Nevertheless, none of the previous studies have focused on deriving the SST coefficients or the Landsat 8 OLI/TIRS data for this region. Furthermore, SST coefficients for the Landsat 8 data have not been provided for coastal regions even in other parts of the global ocean. This might be due to insufficient matchups between the Landsat 8 OLI/TIRS data and in-situ temperature measurements in addition to cloud conditions and other local atmospheric conditions.

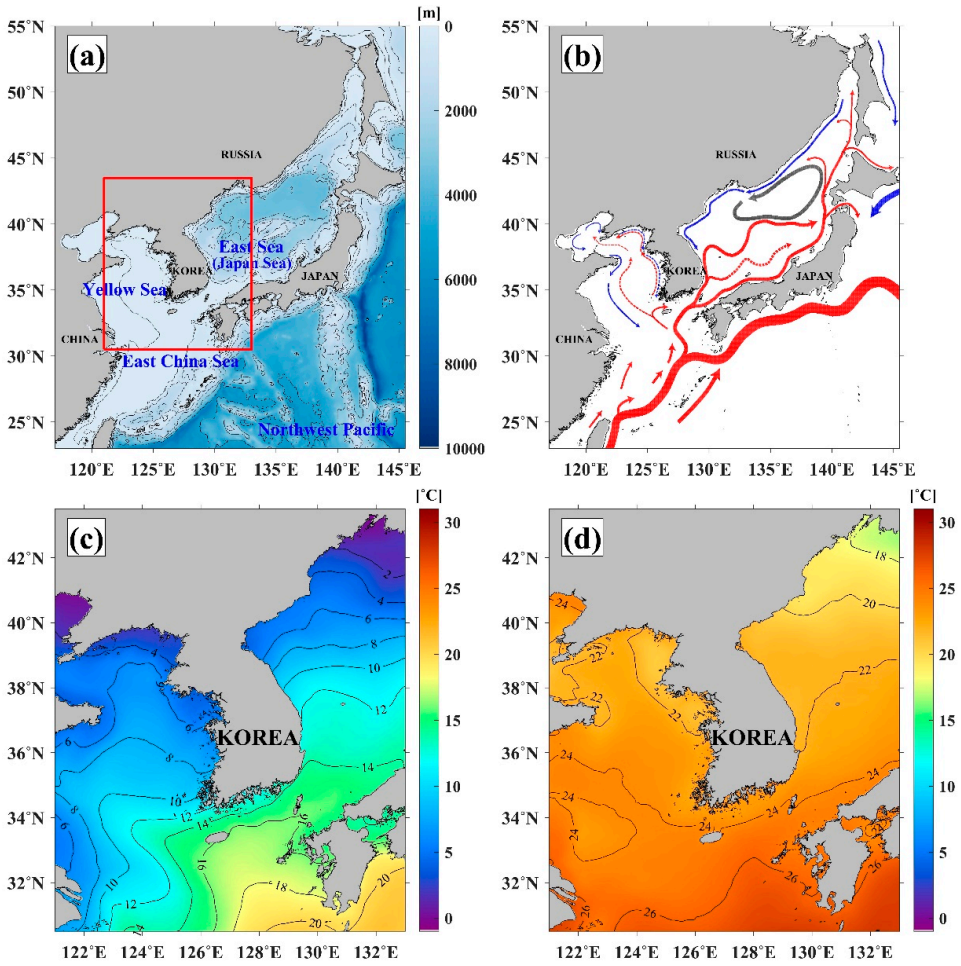

Figure 1. (**a**) Location of the study area with contours of the water depth (m) in the seas around the Northeast Asia including China, Japan, Korea, and Russia, which red box indicates the study area, (**b**) a schematic current map with cold (blue) and warm (red) currents [58], and monthly mean of sea surface temperature (SST) climatology (°C) estimated from the Operational Sea Surface Temperature and Sea Ice Analysis (OSTIA) SST database in the study area from 2002 to 2015 in (**c**) winter (January) and (**d**) summer (July).

2.2. Satellite Data

Landsat 8 has five channels in the visible spectrum (Band 1, Band 2, Band 3, Band 4, and Band 8) and 6 channels in the infrared spectrum (Band 5, Band 6, Band 7, Band 9, Band 10, and Band 11) [44]. The spatial resolution of Landsat 8 OLI/TIRS is 15 m × 15 m in Band 8 (Panchromatic band), 100 m × 100 m in Band 10 and Band 11, and 30 m × 30 m in other bands. The repeat cycle of the Landsat 8 is 16 days and the satellite observes the Korean Peninsula from 02 Universal Time Coordinated (UTC) to 03 UTC. In this study, we selected all of the Landsat 8 OLI/TIRS images over the coastal region of the Korean Peninsula as indicated by the rectangular edges of the images in Figure 2. In total, 276 images from the Landsat 8 OLI/TIRS were processed for the period from 1 April 2013 to 1 August 2017. All Landsat 8 OLI/TIRS data used in this study were the L1TP data obtained from NASA and the United States Geological Survey (USGS) (https://earthexplorer.usgs.gov/).

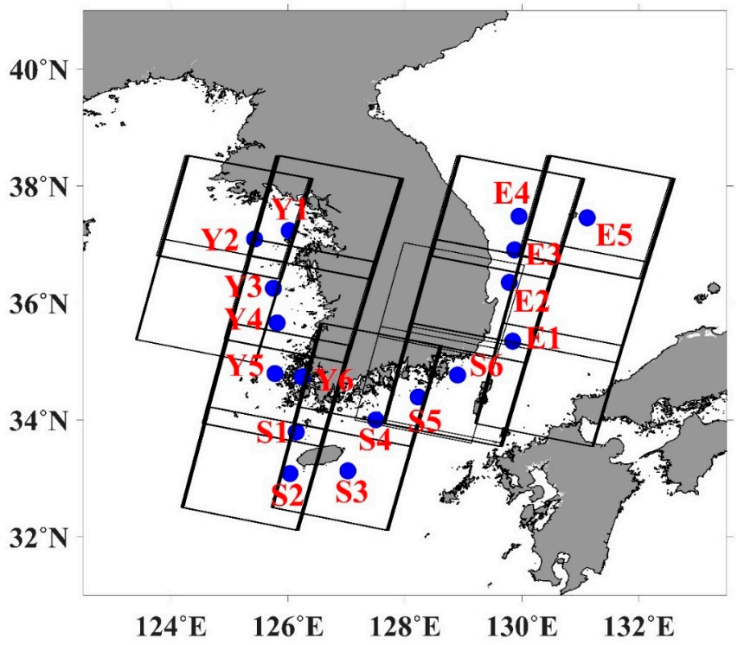

Figure 2. Distribution (black boxes) of the Landsat 8 OLI/TIRS images including the Korea Meteorological Administration (KMA) marine meteorological buoys from 1 April 2013 to 31 August 2017, where the blue circles and the red text around the circles indicate the location and symbol of the KMA marine meteorological buoys, respectively.

In order to address the advantage of high-resolution SST from Landsat 8 OLI/TIRS, we compared the high-resolution SST with the SST data produced from other satellites. We collected the Global Change Observation Mission 1st-Water (GCOM-W1) Advanced Microwave Scanning Radiometer 2 (AMSR-2), the Himawari-8 the Advanced Himawari Imager (AHI), and the NOAA/AVHRR collocated with the Landsat 8 OLI/TIRS data. GCOM-W1/AMSR-2 data used in this study were L2 data obtained from the Remote Sensing System (http://www.remss.com/missions/amsr/), Himawari-8 AHI data used in this study were L2 data obtained from the National Meteorological Satellite Center (NMSC), KMA, and NOAA/AVHRR data used in this study were L2 data obtained from the Research Institute of Oceanography (RIO), Seoul National University (SNU).

2.3. In-Situ Measurements

To derive the coefficients of SST algorithms for SST retrieval from the Landsat 8 OLI/TIRS data, we collected in-situ measurements. Since the Landsat observations have been concentrated at the coastal regions, the data from surface drifters were not sufficient to be used for the estimation and validation of SST coefficients because of the few observations. Korean Meteorological Administration (KMA)

has been operating the marine meteorological buoy stations to monitor the coastal environments around the Korean peninsula as shown in Figure 2. In this study, we use data from 17 KMA marine meteorological buoys, covering the Landsat observational areas, around the coastal regions of the Yellow Sea, the EJS, and in the southern coastal region (https://kma.go.kr/). These KMA buoys observe SST at different depths from 0.1 m to 0.4 m and wind speeds at heights from 3.6 to 4.0 m every hour (Table 1). The equipped thermistors of the buoys have a precision of 0.1 °C and an accuracy of ±0.1 °C for a temperature range from −2 to 40 °C (https://kma.go.kr/). To distinguish the locations of the buoys, we set the symbols of the buoys following the first alphabet of the names of the seas; Y1 to Y6 are buoys in the Yellow Sea, S1 to S6 are in the southern region, and E1 to E5 are in the EJS.

Table 1. Marine meteorological buoy station specification of Korea Meteorological Administration (KMA) in the seas around the Korean Peninsula including the measurement heights of wind speed and sea temperature.

Sea	Station		Location		Observation Height (m)		Date of Installation
	Symbol	Name	Longitude	Latitude	Wind Speed	Sea Temp.	
Yellow Sea	Y1	Deokjeokdo	126.0189°E	37.2361°N	3.6	0.2	Jul. 1996
	Y2	Incheon	125.4289°E	37.0917°N	3.6	0.2	Dec. 2015
	Y3	Oeyeondo	125.7500°E	36.2500°N	3.6	0.2	Nov. 2009
	Y4	Buan	125.8139°E	35.6586°N	3.6	0.2	Dec. 2015
	Y5	Chilbaldo	125.7769°E	34.7933°N	3.6	0.2	Jul. 1996
	Y6	Shinan	126.2417°E	34.7333°N	3.6	0.2	Jun. 2013
Southern region	S1	Chujado	126.1411°E	33.7936°N	4.0	0.1	Jan. 2014
	S2	Marado	126.0333°E	33.0833°N	3.9	0.4	Nov. 2008
	S3	Seogwipo	127.0228°E	33.1281°N	3.6	0.4	Dec. 2015
	S4	Geomundo	127.5014°E	34.0014°N	3.6	0.2	May 1997
	S5	Tongyeong	128.2250°E	34.3917°N	3.6	0.2	Dec. 2015
	S6	Geojedo	128.9000°E	34.7667°N	3.6	0.2	1998. 05.
East Sea Japan Sea (EJS)	E1	Ulsan	129.8414°E	35.3453°N	3.6	0.4	Dec. 2015
	E2	Pohang	129.7833°E	36.3500°N	3.9	0.4	Nov. 2008
	E3	Uljin	129.8744°E	36.9096°N	3.6	0.4	Dec. 2015
	E4	Donghae	129.9500°E	37.4806°N	3.9	0.4	May 2001
	E5	Ulleungdo	131.1144°E	37.4556°N	3.9	0.4	Dec. 2011

2.4. Daily SST Data

For estimating the coefficients using the NLSST formulation, the first-guess SST is needed and can be obtained from the estimated MCSST or climatological SST [18,59]. It is also possible to use other SST products from diverse SST databases. Considering the high-resolution Landsat data and complicated coastal environments for calculating high-resolution SST of less than 100 m, if possible, a high-resolution SST field is preferable as the first-guess SST. Therefore, this study used the OSTIA data provided by the Met Office with 6 km spatial resolution and the Multi-scale Ultra-High Resolution SST (MURSST) data provided by the Group for High-Resolution SST (GHRSST) with 1 km spatial resolution, as the first-guess SST data [60,61]. These SST products from OSTIA and MURSST provide optimally interpolated daily SST, using infrared sensor-based satellites, passive microwave-based satellite data, and in-situ measurements [61,62].

3. Methods

3.1. Removal of Cloud-Contaminated Pixels

Removing pixels contaminated by clouds is important for SST retrieval using infrared sensor-based satellite data. Cloud mask algorithms applicable to the Landsat 8 OLI/TIRS data have been developed by various studies, including the Automated Cloud Cover Assessment (ACCA), the Web Enabled Landsat Data (WELD) Cloud Cover Assessment (CCA) algorithm, the Function of Mask (Fmask) algorithm, and so on [63–65]. In this study, we applied the modified Moderate Resolution Imaging Spectroradiometer (MODIS) Cloud mask algorithm to the Landsat 8 OLI/TIRS data to remove the cloud pixels and the cloud contaminated pixels, prior to the SST retrieval [66,67]. Several tests of this

algorithm have shown that it effectively detects snow and clouds pixels in the Landsat 8 OLI/TIRS images [68]. The Band 3, Band 1, Band 2, Band 6, Band 26, Band 31, and Band 32 of MODIS are substituted respectively with Band 2, Band 4, Band 5, Band 6, Band 9, Band 10, and Band 11 of the Landsat 8 OLI/TIRS. The cloud mask algorithm classifies the pixels of the Landsat 8 OLI/TIRS images into five types (non-vegetated land, vegetated land, snow/ice, water bodies, and clouds). However, in this study we masked the land pixels using the Shuttle Radar Topography Mission (SRTM) Digital Elevation Model (DEM) data (https://earthexplorer.usgs.gov/) and applied the cloud mask algorithm to the pixels for classifying them into snow, ice, water bodies, or clouds (Figure 3).

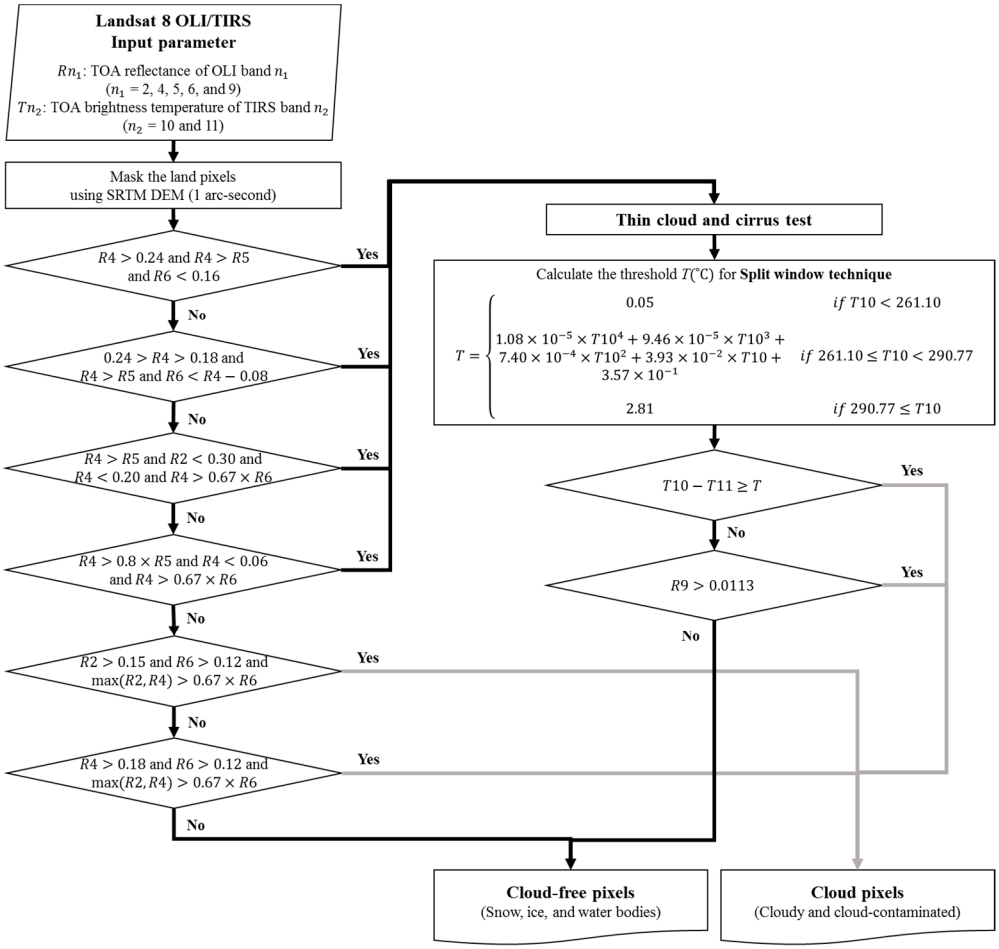

Figure 3. Flow chart of the pixel classification algorithm into the cloud-free pixels, including snow, ice, and water bodies, and cloud pixels, including cloudy and cloud-contaminated (max(a, b): the maximum value of a and b).

Figure 3 shows a series of cloud removal procedures in which the algorithm was developed based on the spectral characteristics of water, snow/ice, and cloud in the visible and shortwave infrared spectrum [69]. The split window test and the cirrus test were added in the algorithm, and the threshold test used in the split window test was calculated by radiative transfer simulations [67]. The threshold of BT difference (BTD) at the 11 μm channel was used to remove large BTD values corresponding to the clouds. In addition, cirrus pixels were removed by applying a threshold of Band 9, which was similar to the cirrus band for the Landsat 8 OLI/TIRS [70,71].

3.2. SST Retrieval Algorithms

For SST retrieval from satellite data, MCSST and NLSST algorithms have been most commonly used, for the 11 and 12 μm channels. These MCSST and NLSST formulations have been used in various

formula with respect to satellite data to various purposes for their uses [72–75]. In case of Landsat data, a simple formulation as the first equations of the MCSST (MCSST1) has been used. However, there is a high possibility that other formulations, containing a term of satellite zenith angle (SZA), would be much more appropriate than the simple MCSST formulation.

The swath of Landsat is relatively narrow with a SZA of up to 7.5 degrees on either side of the satellite orbit path as compared with that of the NOAA/AVHRR or other near-polar orbiting satellites [76–79]. Most of the previous studies have not considered the effect of SZAs in the estimation of SST errors for the Landsat data. Even studies on land surface temperature retrieval and SST retrieval have neglected SZAs under the assumption of nadir observation for all the pixels [50–55,80]. In this study, in order to analyze the effect of the SZA on the SST accuracy, we classified into the two cases, including considering and neglecting the SZA-related terms both in the MCSST and the NLSST formulations in Table 2. Therefore, we proposed eight SST equations, two cases for the MCSST and four cases for the NLSST with respect to the input data of first-guess SST and consideration of the SZA. For each formulation, we derived the SST coefficients and assessed the accuracy of each equation.

Table 2. Formula based on MCSST and NLSST algorithms (T_{11} and T_{12}: Brightness temperature at 11 μm and 12 μm (in Celsius), T_{sfc1}, T_{sfc2}, and T_{sfc3}: MCSST, OSTIA SST, and MURSST as first-guess SST (in Celsius), θ: satellite zenith angle, a_1, a_2, a_3, and a_4: regression coefficients).

Algorithm	Symbol	Equation
MCSST	MCSST1	$\mathrm{SST} = a_1T_{11} + a_2(T_{11} - T_{12}) + a_3$
	MCSST2	$\mathrm{SST} = a_1T_{11} + a_2(T_{11} - T_{12}) + a_3(T_{11} - T_{12})(\sec\theta - 1) + a_4$
NLSST	NLSST1	$\mathrm{SST} = a_1T_{11} + a_2T_{sfc1}(T_{11} - T_{12}) + a_3$
	NLSST2	$\mathrm{SST} = a_1T_{11} + a_2T_{sfc2}(T_{11} - T_{12}) + a_3$
	NLSST3	$\mathrm{SST} = a_1T_{11} + a_2T_{sfc3}(T_{11} - T_{12}) + a_3$
	NLSST4	$\mathrm{SST} = a_1T_{11} + a_2T_{sfc1}(T_{11} - T_{12}) + a_3(T_{11} - T_{12})(\sec\theta - 1) + a_4$
	NLSST5	$\mathrm{SST} = a_1T_{11} + a_2T_{sfc2}(T_{11} - T_{12}) + a_3(T_{11} - T_{12})(\sec\theta - 1) + a_4$
	NLSST6	$\mathrm{SST} = a_1T_{11} + a_2T_{sfc3}(T_{11} - T_{12}) + a_3(T_{11} - T_{12})(\sec\theta - 1) + a_4$

3.3. Calculation of Satellite Zenith Angle

The swath width of the Landsat 8 OLI/TIRS satellite is relatively small, hence, many studies usually assume that the viewing zenith angle α as the SZA, without considering the curvature of the Earth. In this case, the SZA is up to about 7.5 degrees, but it is essential to calculate the precise SZA for accurate SST retrieval. Therefore, in this study, in order to obtain the accurate SZA, we calculated it with by considering the curvature of the Earth [81]. Figure 4 shows the schematic diagram of the calculation of SZA of the Landsat 8 satellite. In the schematic diagram, the target pixel T for SZA retrieval is calculated using the distance d from the sub-satellite point S. Assuming the radius of the Earth R is 6371 km, the center angle of the Earth β can be calculated based on the law of the arc as follows:

$$\beta(\mathrm{rad}) = \frac{d}{R} \tag{1}$$

If the altitude h of the Landsat 8 OLI/TIRS is assumed to be 705 km, it is possible to calculate the distance b from the satellite to the target pixel according to the second law of cosine:

$$\mathrm{b(km)} = \sqrt{R^2 + (R+h)^2 - 2R(R+h)\cos\beta} \tag{2}$$

Finally, we calculate γ based on the law of sine and the SZA, defined as 180°-γ:

$$\frac{R+h}{\sin\gamma} = \frac{b}{\sin\beta} = \frac{R}{\sin\alpha} \tag{3}$$

In this way, the SZA value of each pixel was calculated for the ranges from satellite orbit path with zero degree to the end points on the left and the right side with the angles of about ±8.4 degrees.

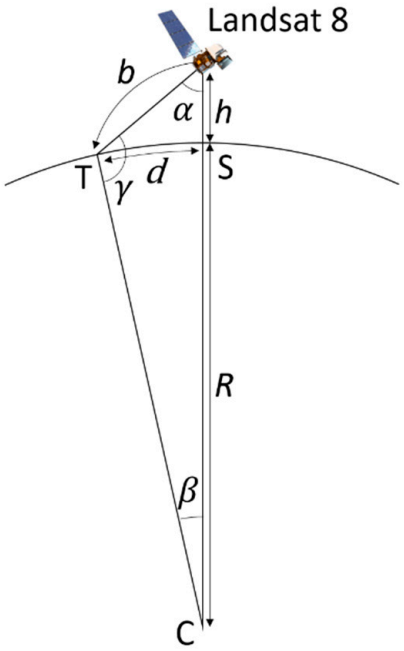

Figure 4. Schematic diagram for geographic definition relating the along-scan distance d to the viewing angle α, where C is the center of the Earth, S is the sub-satellite point, T is the location of target pixel, R is the radius of the Earth, and h is the satellite altitude by following [81].

3.4. Quality Control of In-Situ Measurements

The buoys, used in this study for calculation of the SST coefficients and their validation, have been providing marine environmental observations for a long period (Table 1). The in-situ measurements from the KMA marine meteorological buoy are distributed primarily after the QC process, however, some anomalous observations are produced unexpectedly as well. Therefore, a QC process is necessary to accurately calculate and verify the SST data [82]. For this, a series of QC methods developed by the KMA were applied to the in-situ data. This method consists of sequential tests to remove low-quality data and outliers for each individual buoy data. The buoy data for QC should be composed of at least ten measurements within a day and the difference between the maximum and minimum SST within a day should be greater than 0 °C and less than 4 °C for the monitoring of daily SST fluctuations. For the time-continuity test, the difference of SST from the daily mean should be less than three standard deviations of the temperatures within 1 and 4 days. The standard deviation of SST within 4 days should be less than 2 °C. Figure 5 shows an example of SST QC results before and after applying the QC process to the buoy measurements. Prior to the QC process, the time-series of the buoy temperatures revealed abnormal lower peaks and higher peaks by deviating from general SST fluctuations (Figure 5a,b). After applying a QC process similar to a de-spiking procedure, the unusual peaks were completely eliminated as shown in Figure 5c–f.

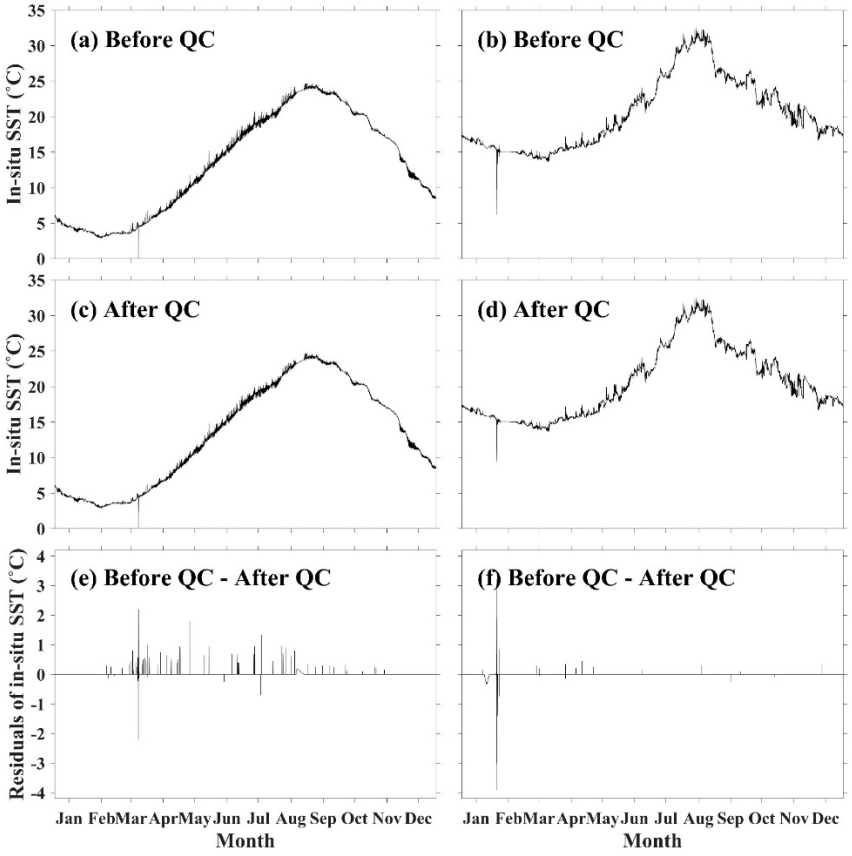

Figure 5. Examples of time series of in-situ sea temperature (°C) observed by KMA buoys (**a**,**b**) before and (**c**,**d**) after QC procedure to remove abnormal temperatures and (**e**,**f**) the comparison of residual (before QC procedure and after QC procedure).

4. Results

4.1. Matchup Data

Figure 6a shows the spatial distribution of the number of matchup data at the buoy locations off the coast of the Korean peninsula from 1 April 2013 to 31 August 2017. The total number of the matchup data between the Landsat 8 OLI/TIRS images and the KMA ocean buoy data amounted to 320 and the largest number of matchups was 43, for the buoy Y1. The smallest number of the matchups was 6, for the buoys Y2 and S3 (Figure 6a). During the study period over five years, there were no matchups between the Landsat 8 data and the buoy data in some months (June 2013, June 2014, August 2014, January 2015, and June 2016) due to the mask associated with clouds, as shown in Figure 6b. The month-year plot of the matchup numbers in Figure 6b exhibits the maximum number of the matchups of 14 on April 2017. The in-situ temperatures of the matchup database ranged from 3.2 to 30.2 °C and the maximum frequency of occurrence of in-situ temperatures was in the range of 14.5 to 15.5 °C (Figure 6c). The KMA ocean buoys measure not only the sea water temperature at a depth of less than 0.4 m but also the wind speed. The in-situ wind speed of the matchup database ranged from 0.1 to 12.2 m s^{-1}, and the maximum frequency of occurrence of the in-situ wind speed was located at the bin from 4.3 to 4.7 m s^{-1} (Figure 6d).

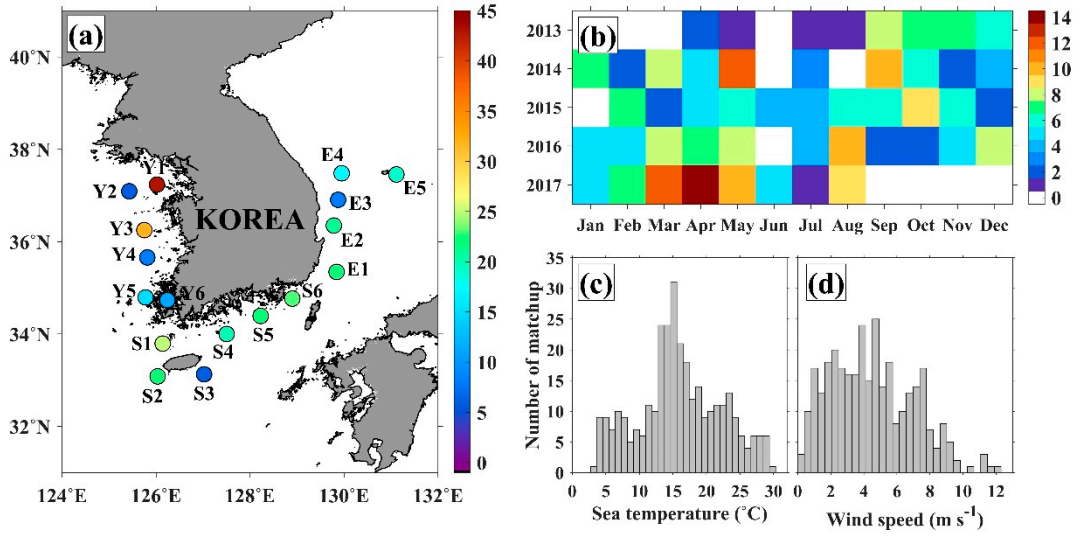

Figure 6. (**a**) The number of matchup data for each KMA marine meteorological buoy in the seas around the Korean Peninsula, (**b**) the number of Landsat 8 OLI/TIRS image acquisition from 1 April 2013 to 31 August 2017, and the histograms of the matchup data with respect to (**c**) sea temperature and (**d**) wind speed.

4.2. Derivation of SST Coefficients

Figure 7 shows the comparison of satellite SSTs, estimated using MCSST and NLSST, with the in-situ SST. The accuracy of SST when using each algorithm of MCSST1, MCSST2, NLSST1, NLSST2, NLSST3, NLSST4, NLSST5, and NLSST6 showed the RMSEs of 0.72 °C, 0.71 °C, 0.66 °C, 0.61 °C, 0.63 °C, 0.65 °C, 0.59 °C, and 0.62 °C, respectively (Figure 7). All the algorithms showed that the biases are close to zero without any noticeable trend (Figure 7, Table 3). As can be seen from the distribution of the number frequencies in the comparison plots, the scattering index (SI) of each algorithm (MCSST1, MCSST2, NLSST1, NLSST2, NLSST3, NLSST4, NLSST5, and NLSST6) was 0.0450, 0.0444, 0.0416, 0.0382, 0.0397, 0.0407, 0.0374, and 0.0387, respectively. Their correlation coefficients (R) were relatively high amounting to 0.9933, 0.9935, 0.9943, 0.9952, 0.9948, 0.9945, 0.9954, and 0.9950, respectively, and their *p*-values were 1.07E-299, 7.66E-302, 1.02E-310, 1.20E-322, 2.92E-317, 8.60E-314, 0, and 1.65E-320, respectively. Comparison results showed that the NLSST5 algorithm seems to be relatively accurate with a RMSE of about 0.59 °C as compared with other algorithms.

Table 3. Coefficients of MCSST1, MCSST2, NLSST1, NLSST2, NLSST3, NLSST4, NLSST5, and NLSST6 algorithms and root-mean-square error (RMSE) and bias error.

Algorithm	Symbol	Coefficients				RMSE (°C)	Bias (°C)
		a_1	a_2	a_3	a_4		
MCSST	MCSST1	0.9767	1.8362	0.0699		0.72	−2.04E-15
	MCSST2	0.9742	1.7742	32.9868	0.0637	0.71	−3.54E-15
NLSST	NLSST1	0.9042	0.0824	1.4408		0.66	1.28E-15
	NLSST2	0.8965	0.0842	1.5122		0.61	3.77E-16
	NLSST3	0.9009	0.0817	1.4808		0.63	1.47E-15
	NLSST4	0.9026	0.0802	32.0333	1.3990	0.65	3.39E-15
	NLSST5	0.8953	0.0819	32.3713	1.4672	0.59	1.10E-15
	NLSST6	0.8992	0.0793	35.3699	1.4341	0.62	1.77E-15

Table 3 summarizes the accuracy and coefficients of the SST retrieval algorithm. Coefficients of the 11 μm BT term in the MCSST algorithms were about 0.97, closer to 1.0 than the NLSST algorithms. For the Landsat 8 OLI/TIRS, the coefficient of SZA term was about 32 to 35 for MCSST2, NLSST4,

NLSST5, and NLSST6 algorithms, which was much higher than that of the MCSST and the NLSST algorithms using other algorithms for other satellites. Since the maximum value of SZA is up to about 8.4, the SZA term is close to 0. The high coefficients of these algorithms are believed to reflect the role of the SZA term in the SST retrieval equations. If the SZA term was neglected from the formulations, the accuracy of the NLSST with an RMSE of 0.61–0.66 °C was better than that of the MCSST with an RMSE of 0.72 °C. The cases where the SZA terms were considered, such as MCSST2, NLSST4, NLSST5, and NLSST6, were evaluated to be more accurate than those without the SZA effect considered in the formulation. For the first-guess SST, the input of OSTIA SST data was more accurate than the use of the estimated SST from the MCSST equation and MURSST. The accuracy of the SST derived from the Landsat 8 OLI/TIRS varied depending on the algorithms as well as the first-guess SST used as input data for the SST formulations. The RMSE values of the Landsat 8 OLI/TIRS given in Table 3 were quite similar to those from the numerous previous studies using other satellites [25,26,83].

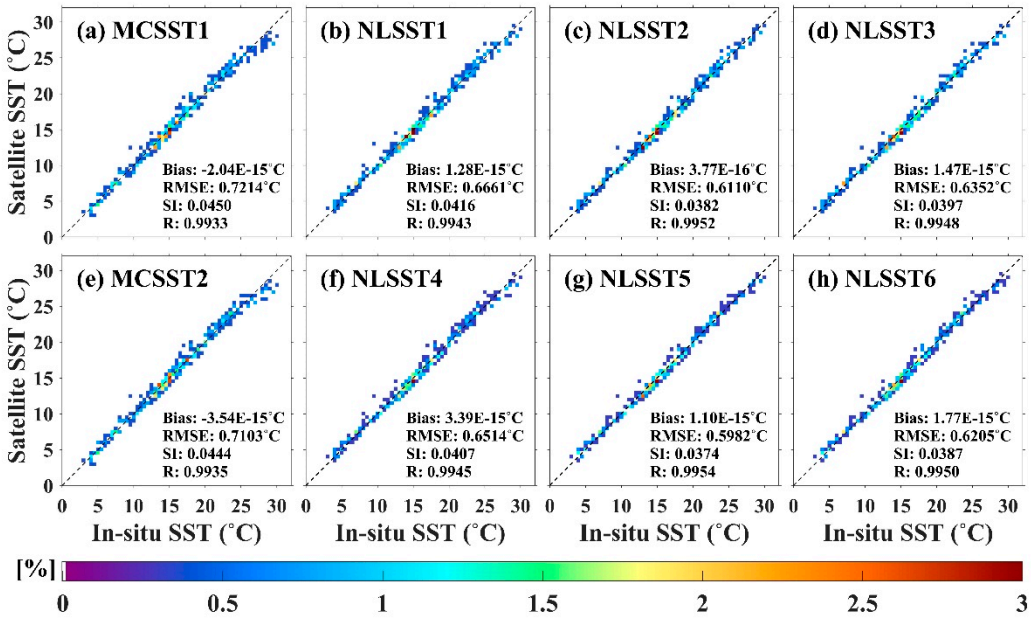

Figure 7. Comparison between satellite derived SST and in-situ temperature using (**a**,**e**) MCSST and (**b**,**c**,**d**,**f**,**g**,**h**) NLSST algorithms, where the color represents the percentage of the data to the total number of matchup points in a bin of 0.5 °C × 0.5 °C. Bias, root-mean-square error (RMSE), scatter index (SI), and correlation coefficient (R) are given in each plot.

4.3. High-Resolution SST

The Landsat 8 OLI/TIRS has an exceptionally high spatial resolution compared with other satellites used for SST retrieval. Using the coefficients for Landsat 8 derived in this study, SSTs were estimated for the southeastern coastal region of the Korean peninsula. These SSTs were compared with SSTs from the OSTIA, the MURSST, the GCOM-W1/AMSR-2, the Himawari-8 AHI, and the NOAA/AVHRR (Figure 8). The measured SSTs in S05 and S06 buoys were 13.7 °C and 14.8 °C at 02 UTC on 19 April 2019, respectively. Figure 8a shows the SST distribution from the OSTIA on 19 April 2016 and the collocated SSTs with each buoy were 14.1 °C and 14.6 °C, respectively. Figure 8b shows the SST distribution from the MURSST on 19 April 2016 and the collocated SSTs with each buoy were 14.0 °C and 14.2 °C, respectively. Figure 8c shows the SST distribution from the GCOM-W1/AMSR-2 at 05UTC on 19 April 2016. Due to its low spatial resolution of about 25 km and the effect of land on microwave measurements, there were only a few pixels with SSTs without any observations in the coastal area from 50 km to 100 km distance from the shoreline [84,85]. This implies that the microwave measurements are inappropriate to observe the SSTs of the coastal region. On the contrary, the Himawari-8 AHI produced SSTs with relatively high spatial resolution of about 2 km as shown in Figure 8d and the

collocated SSTs with each buoy were 14.4 °C and 14.9 °C at 02 UTC on 19 April 2016, respectively. The NOAA/AVHRR data with a spatial resolution of about 1.1 km revealed more detailed structure of SST distribution including the contrast differences of temperatures at the frontal region between the onshore and the offshore regions and the collocated SSTs with each buoy were 14.3 °C and 14.8 °C at 05 UTC on 19 April 2016, respectively (Figure 8e).

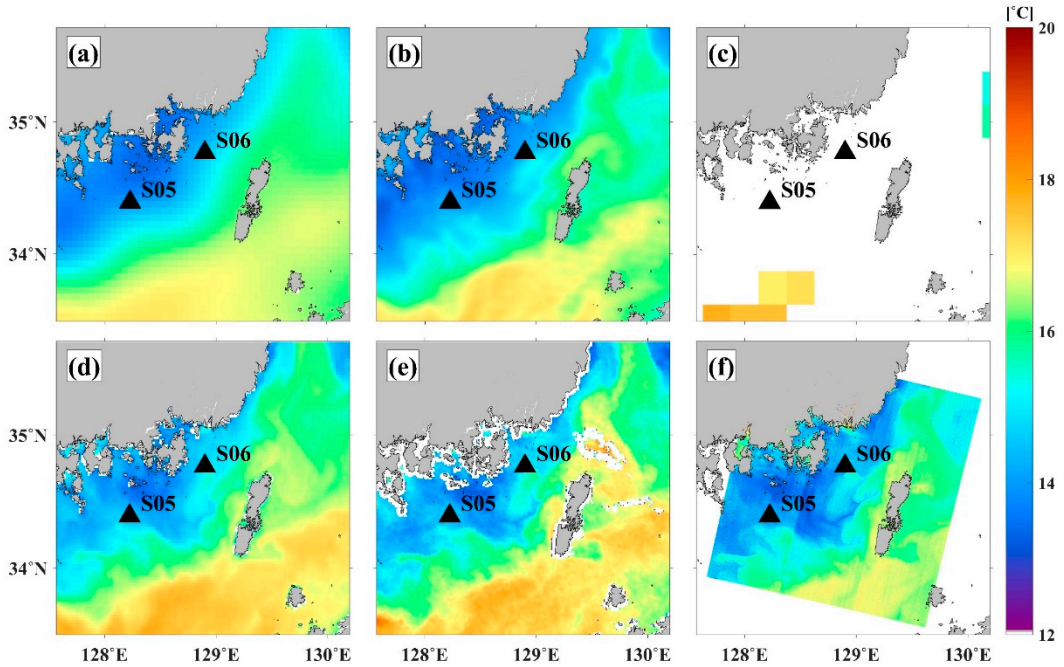

Figure 8. Distributions of SST derived from (**a**) OSTIA SST daily composite on 19 April 2016, (**b**) MURSST daily composite on 19 April 2016, (**c**) GCOM-W1/AMSR-2 observed at 05 UTC on 19 April 2016, (**d**) Himawari-8 AHI observed at 02 UTC on 19 April 2016, (**e**) NOAA-19 AVHRR observed at 05 UTC on 19 April 2016, and (**f**) Landsat 8 OLI/TIRS observed at 02 UTC on 19 April 2016 using the NLSST5 algorithm, where the black triangles indicate the KMA buoys.

The land pixels in Landsat 8 OLI/TIRS data were masked using SRTM DEM data prior to SST retrieval and the collocated SSTs with each buoy were 14.3 °C and 14.8 °C, respectively. Coastal SST patterns of the Landsat 8 (Figure 8f) illustrated more detailed spatial structures compared to other SST products (Figure 8a–e). Since the SSTs from the databases (AMSR-2, Himawari-8, NOAA-19, and Landsat 8) were observed at different times from 02 UTC to 05 UTC, they might be different due to diurnal variations of surface temperatures depending on the observation times during a day. Moreover, the composite products of OSTIA and MURSST represent average values of SSTs at that day. Nevertheless, most of the SSTs presented similar SSTs with relatively small differences of less than 1.6 °C. It is notable that the SSTs of Landsat 8 were well produced in the offshore region as well as along the coastline and around many complicated islands as shown in Figure 8f. This demonstrated the capability and usefulness of Landsat 8 data at the coastal regions including the estuarine regions. Thus, the comparison addresses the importance of using high-resolution SST data for coastal regions with very complicated temperature variations.

5. Discussion

5.1. Effect of Atmospheric Moisture

The 11 μm channel is regarded to be a clean infrared atmospheric-window channel because it has limited absorption by atmospheric water vapor. On the contrary, the radiance at the 12 μm channel is relatively higher absorbed by atmospheric water vapor. Therefore, the BTD values between these

two channels can reflect the absorption effect of the water vapor in the air [86]. The SST retrieval algorithms used these BTD terms to consider the effects of atmospheric water vapor on the estimation of SST. Figure 9 shows the SST errors; satellite SST minus in-situ temperature, as a function of the BTD. One of conspicuous features is that both the MCSST1 and the MCSST2 algorithms resulted in obvious biases with significant underestimation of lower than −2.0 °C in the range of BTD greater than 2.0 K (Figure 9a,b). By contrast, these errors were considerably reduced in cases of the NLSST algorithms as shown in the algorithms (NLSST1, NLSST2, NLSST3, and NLSST4) from Figure 9c to Figure 9f. It is expected that the NLSST formulations would reduce the SST errors arising from the amount of water vapor in the air. Thus, the non-linear approaches based on the NLSST formulations are concluded to be better than the MCSST algorithms.

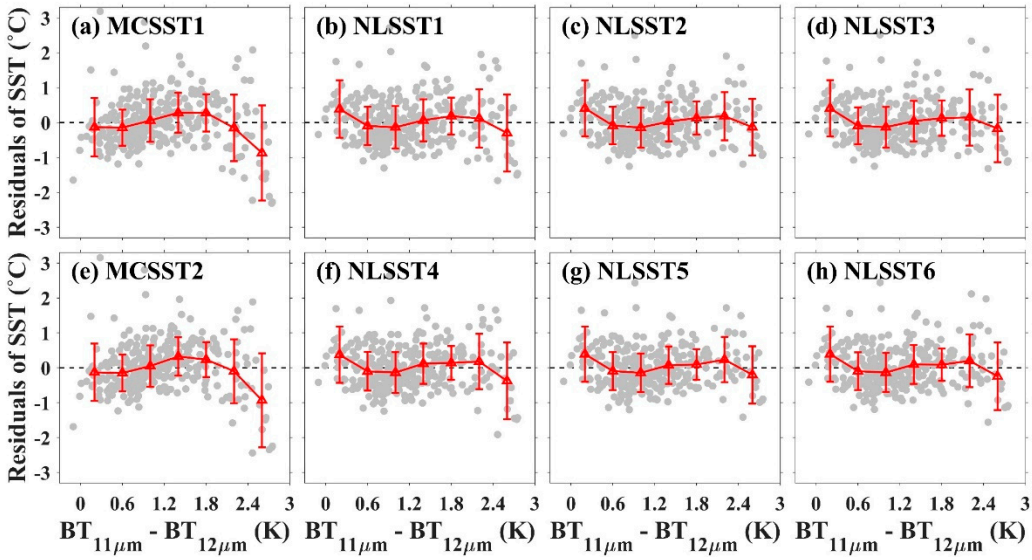

Figure 9. Comparison of residuals (Landsat 8 OLI/TIRS SST – buoy SST) using (**a**) MCSST1, (**b**) NLSST1, (**c**) NLSST2, (**d**) NLSST3, (**e**) MCSST2, (**f**) NLSST4, (**g**) NLSST5, and (**h**) NLSST6 with brightness temperature difference between 11 μm and 12 μm, where the red points and bars represent the mean value and standard deviation of SST errors for each interval, respectively.

5.2. Effect of SZA

As SZA increases, the atmospheric layer thickness through which the signal emitted from sea surface pass increases, affecting the intensity of the signal reaching the satellite. Accordingly, the SZA is one of the most important elements to accurately derive SST, as the atmospheric absorption effect is proportional to the SZA [87]. Most of the wide-scanning sensors such as the NOAA/AVHRR with a swath angle of 55 degrees in both sides have considered the effect of the SZA [25]. Since the Landsat sensors have very narrow viewing angles from −8.4 degrees to the left and 8.4 degrees to the right based on the satellite orbit path, the effect of viewing angle has been neglected in the SST retrieval procedures for a long time [46,51–54]. However, the accuracy assessment of this study showed that the algorithms including the SZA term estimated SST with better performance. Regardless of the algorithms or the different use of the first-guess SST, the inclusion of the SZA reduced the SST errors.

To evaluate the performance rate of the improvement in SST when the SZA term is included, we estimated the percentage of the SST differences with respect to the SZA (Figure 10). In case of the MCSST errors, the percentage was estimated with the errors, MCSST2 with the SZA term - MCSST1 without the SZA term divided by the MCSST2. Positive (Negative) angles of the SZA values correspond to the SZA on the right (left) side from the central ground track of the satellites. The enhanced percentages of the MCSST case showed a symmetric structure as indicated in Figure 10a. The maximum decrease was 0.75% in the range from −1 to 1 degree, and the maximum increase was 1.49% in the range from 7 to 9 degree. By adding the SZA term, the estimated SST was improved in the opposite direction based on

±4 degrees, resulting in an increase of about 0.1 °C in RMSE. The accuracies of the SSTs on the edges with high SZA of about −8 or 8 degrees improved over 1% by reaching 3%. Other cases of the NLSST formulations also revealed improved capability of the algorithms in reducing the errors when the SST formulations included the SZA term. This implies that the SST formulation should include the SZA to estimate more accurate SST from the Landsat 8 data in spite of its narrow swath width.

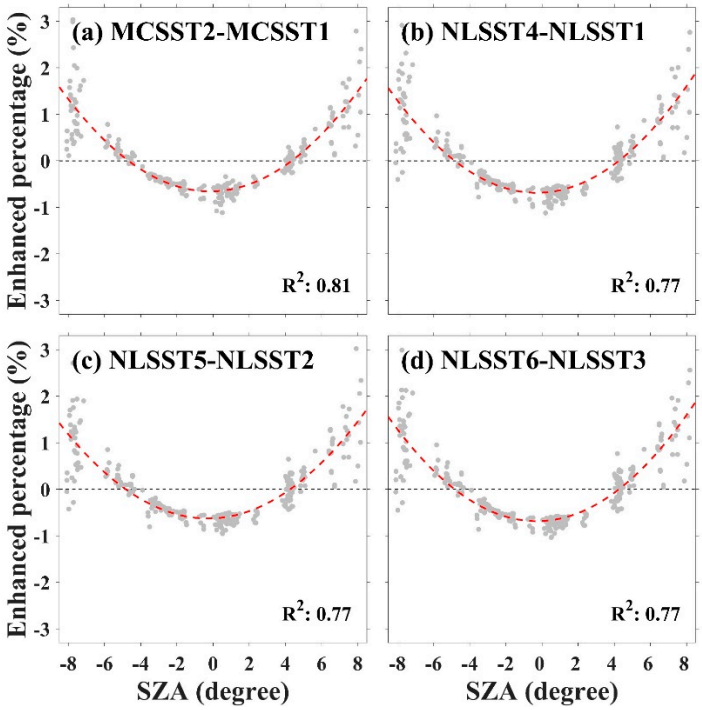

Figure 10. Comparison of enhanced percentage with satellite zenith angle (SZA) (enhanced percentage: (SST with SZA term – SST without SZA term) / SST with SZA term) using (**a**) MCSST2 and MCSST1, (**b**) NLSST4 and NLSST1, (**c**) NLSST5 and NLSST2, and (**d**) NLSST6 and NLSST3, where the red dashed lines represent the 2nd order polynomial fitted lines.

5.3. Effect of Wind Speed

Although we derived the SST coefficients by regressing the satellite BT values to the buoy temperatures, the SST is different from the skin SST measured at the thin layer that is affected by the heat transfer and diffusion from the atmosphere ocean boundary layer [88]. Since the temperature sensors of the buoys are located at different depths from 0.2 to 0.4 m, the retrieved SST might have a possibility to be affected by the winds, as pointed out by the previous studies [89–92]. Therefore, we tested if the derived SSTs from the Landsat 8 have any relation to the wind speed.

Figure 11 shows the difference between buoy temperature and SST derived from the Landsat 8 OLI/TIRS according to the wind speed, for the eight cases from MCSST1 to NLSST6. Regardless of the algorithms or the different first-guess SSTs, no distinct bias errors were observed in the range of wind speeds higher than 2 m s^{-1}. However, the Landsat 8 OLI/TIRS SSTs tended to be overestimated in the range of wind speeds below 2 m s^{-1} as indicated in all plots in Figure 11 [92,93]. Overall, an average positive bias of 0.63 °C was found in the range of wind speeds below 2 m s^{-1}.

Since the Landsat satellite observes the sea surface at 11 to 12 AM on local time, the difference between the bulk SST and the skin SST could be directly affected by the solar thermal energy, which causes the increase in the skin SST at this time [94]. At low wind speeds, the difference between the bulk SST and the skin SST is large because of the weak mixing in the upper marine layer, however at high wind speeds, the mixing of the upper layer is active and the difference between the skin SST and the bulk SST decreases [95]. This trend is evident in the previous validation studies of

other satellite-derived SSTs [26,59,96]. In this study, it was confirmed that the error characteristics of SST derived from the Landsat 8 OLI/TIRS were clearly shown at daytime with low wind speed. This addresses the significant imprint of low wind condition on satellite SSTs, which produces the overestimation, especially in a range of less than 2 m s^{-1}.

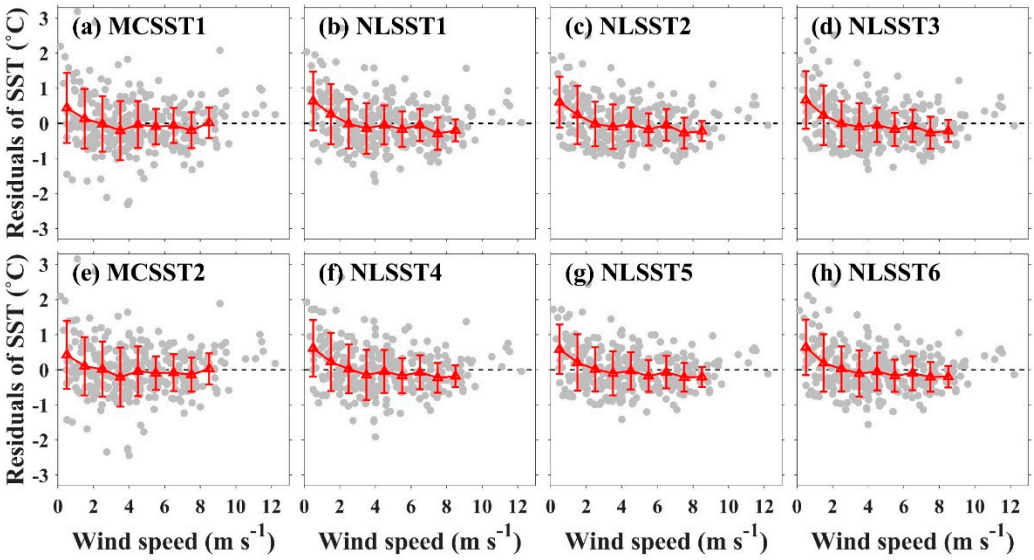

Figure 11. Comparison of residuals (Landsat 8 OLI/TIRS SST – buoy SST) using (**a**) MCSST1, (**b**) NLSST1, (**c**) NLSST2, (**d**) NLSST3, (**e**) MCSST2, (**f**) NLSST4, (**g**) NLSST5, and (**h**) NLSST6 with wind speed, where the red points and bars represent the mean value and standard deviation of SST errors for each interval, respectively.

6. Summary and Conclusions

In order to calculate the SST coefficients for the Landsat 8 OLI/TIRS, this study produced the matchup database between the Landsat 8 data and the KMA marine meteorological buoy measurements for the coastal region around the Korean Peninsula. A total number of 276 Landsat 8 OLI/TIRS images were used to produce 320 matchup data for the period from April 2013 to August 2017. The curvature of the Earth was taken into account for estimating more accurate SZA with a range of about ±8.4 degrees, which was a little wider than the angles calculated by the previous studies under the assumption of a flat sea surface, within the relatively narrow swath of the Landsat 8. The SST algorithms were classified into MCSST1, MCSST2, NLSST1, NLSST2, NLSST3, NLSST4, NLSST5, and NLSST6 depending on the uses of SZA terms or the first-guess SST. These algorithms produced RMSEs of 0.72 °C, 0.71 °C, 0.66 °C, 0.61 °C, 0.63 °C, 0.65 °C, 0.59 °C, and 0.62 °C, respectively. Among the algorithms, the smallest error in terms of RMSE and bias was found for the NLSST5 using SZA, with OSTIA SST as the first-guess SST rather than MCSST and MURSST.

Characteristics of the retrieved SSTs were analyzed by investigating the effects of the SZA, the absorption of atmospheric water vapor, and the wind speeds on the SST. The satellite-derived MCSSTs had a tendency to be underestimated at relatively high moist condition of greater than 2 K as inferred from the differences between the 11 μm and 12 μm channel BTs. Such errors of MCSSTs were reduced in the case of the NLSST formulations by applying the SZA and the use of the proper first-guess SST. The SST errors revealed the quadratic dependence on the SZA values from the nadir to the edge of the swath. After the inclusion of SZA term in the SST estimation, the SST results were moderately improved by less than 3% as compared with prior equations without the angle term. The error analysis due to the wind speeds showed that, the SST errors were amplified as the wind speeds became weak at a range of less than 2 m s^{-1}. This has been reported to be associated with the skin-bulk temperature differences and solar insolation under weak wind condition [86,89]. When the SST coefficients calculated from the

matchup data from April 2013 to August 2016 were applied to the data from September 2016 to August 2017, the RMSE was less than about 0.7 °C. Therefore, it is expected that similar accuracy would be maintained even if the SST coefficients calculated in this study were applied to the Landsat 8 OLI/TIRS data; subsequent to other periods or other coastal regions.

The previous Landsat satellites observed using one thermal infrared band, but the Landsat 8 OLI/TIRS was classified into 11 and 12 μm bands in the thermal infrared band. Therefore, the most commonly used MCSST and NLSST for SST retrieval are available, but SST coefficients optimized for the Landsat 8 OLI/TIRS data have not been developed. In addition, this study considered the effect of the SZA in the SST retrieval formulations. The repeat cycle of the Landsat with a small swath width is much longer than other polar-orbiting satellites (e.g., MODIS and VIIRS) with complete global coverage every day. Moreover, it could be difficult for SST retrieval using Landsat to be applied to the areas with regional characteristics of intense cloud cover such as the coastal regions off California, Peru, or Chile. Nevertheless, by this study, when the SST algorithm suitable for Landsat 8 OLI/TIRS is established, we expect to be able to study sub-kilometer small scale ocean phenomena in the coastal region.

Since the Korean coastal region has a variety of oceanic phenomena in terms of time and space scales, with fronts, eddies, tidal currents, river discharge, and estuary, the SST coefficients derived in this study might be applicable to SST derivation for other coastal regions of the global ocean as well, especially for the regions without any local SST coefficients for the Landsat 8 data. For more extensive and operational use of the Landsat 8 OLI/TIRS derived SSTs, it is important to continuously monitor and understand the error characteristics of the SST using in-situ measurements in diverse ocean regions. If the validation studies in various sea areas are conducted with satisfactory results, it is expected that the present SST algorithms and coefficients could be further improved in the future and be extensively used for studying small-scale ocean phenomena in the coastal regions including estuarine regions. Based on the local error characteristics in these studies, it is possible to reduce the regional SST errors through regional optimization for accurate SST retrieval procedures.

Author Contributions: Conceptualization, K.-A.P.; data curation, J.-C.J.; methodology, K.-A.P. and J.-C.J.; writing—original draft preparation, J.-C.J.; writing—review and editing; K.-A.P. and J.-C.J.

Funding: This work was funded by the Korea Meteorological Administration Research and Development Program under Grant KMI2018-05110.

Acknowledgments: OSTIA SST data and MURSST data were provided by GHRSST. GCOM-W1/AMSR-2 data were obtained from Remote Sensing System (http://www.remss.com/missions/amsr/). Landsat 8 OLI/TIRS data were obtained from USGS (https://earthexplorer.usgs.gov/). NOAA/AVHRR data were obtained from RIO, SNU. Himawari-8 data were obtained from NMSC, KMA.

Conflicts of Interest: The authors declare no conflict of interest.

References

1. Corlett, G.K.; Barton, I.J.; Donlon, C.J.; Edwards, M.C.; Good, S.A.; Horrocks, L.A.; Llewellyn-Jones, D.T.; Merchant, C.J.; Minnett, P.J.; Nightingale, T.J.; et al. The accuracy of SST retrievals from AATSR: An initial assessment through geophysical validation against in situ radiometers, buoys and other SST data sets. *Adv. Space Res.* **2006**, *37*, 764–769. [CrossRef]
2. Dash, P.; Ignatov, A.; Kihai, Y.; Sapper, J. The SST quality monitor (SQUAM). *J. Atmos. Ocean. Technol.* **2010**, *27*, 1899–1917. [CrossRef]
3. Ullman, D.S.; Cornillon, P.C. Evaluation of front detection methods for satellite-derived SST data using in situ observations. *J. Atmos. Ocean. Technol.* **2000**, *17*, 1667–1675. [CrossRef]
4. Park, K.A.; Chung, J.Y.; Kim, K. Sea surface temperature fronts in the East (Japan) Sea and temporal variations. *Geophys. Res. Lett.* **2004**, *31*. [CrossRef]
5. Park, K.A.; Cornillon, P.; Codiga, D.L. Modification of surface winds near ocean fronts: Effects of Gulf Stream rings on scatterometer (QuikSCAT, NSCAT) wind observations. *J. Geophys. Res.* **2006**, *111*. [CrossRef]
6. O'Neill, L.W.; Chelton, D.B.; Esbensen, S.K.; Wentz, F.J. High-resolution satellite measurements of the atmospheric boundary layer response to SST variations along the Agulhas Return Current. *J. Clim.* **2005**, *18*, 2706–2723. [CrossRef]

7. Park, K.-A.; Cornilon, P.C. Stability-induced modification of sea surface winds over Gulf Stream rings. *Geophys. Res. Lett.* **2002**, *29*. [CrossRef]
8. Casey, K.S.; Cornillon, P. Global and regional sea surface temperature trends. *J. Clim.* **2001**, *14*, 3801–3818. [CrossRef]
9. Minnett, P.J.; Corlett, G.K. A pathway to generating Climate Data Records of sea-surface temperature from satellite measurements. *Deep Sea Res. II* **2012**, *77*, 44–51. [CrossRef]
10. Merchant, C.J.; Embury, O.; Rayner, N.A.; Berry, D.I.; Corlett, G.K.; Lean, K.; Veal, K.L.; Kent, E.C.; Llewellyn-Jones, D.T.; Remedios, J.J.; et al. A 20 year independent record of sea surface temperature for climate from Along-Track Scanning Radiometers. *J. Geophys. Res.* **2012**, *117*. [CrossRef]
11. Anding, D.; Kauth, R. Estimation of sea surface temperature from space. *Remote Sens. Environ.* **1970**, *1*, 217–220. [CrossRef]
12. Prabhakara, C.; Dalu, G.; Kunde, V.G. Estimation of sea surface temperature from remote sensing in the 11-to 13-µm window region. *J. Geophys. Res.* **1974**, *79*, 5039–5044. [CrossRef]
13. McMillin, L.M. Estimation of sea surface temperature from two infrared window measurements with different absorptions. *J. Geophys. Res.* **1975**, *80*, 5113–5117. [CrossRef]
14. Bernstein, R.L. Sea surface temperature estimation using the NOAA 6 satellite advanced very high resolution radiometer. *J. Geophys. Res.* **1982**, *87*, 9455–9465. [CrossRef]
15. McMillin, L.M.; Crosby, D.S. Theory and validation of the multiple window sea surface temperature technique. *J. Geophys. Res.* **1984**, *89*, 3655–3661. [CrossRef]
16. McClain, E.P.; Pichel, W.G.; Walton, C.C. Comparative performance of AVHRR-based multichannel sea surface temperatures. *J. Geophys. Res.* **1985**, *90*, 11587–11601. [CrossRef]
17. Walton, C.C. Nonlinear multichannel algorithms for estimating sea surface temperature with AVHRR satellite data. *J. Appl. Meteorol.* **1988**, *27*, 115–124. [CrossRef]
18. Walton, C.C.; Pichel, W.G.; Sapper, J.F.; May, D.A. The development and operational application of nonlinear algorithms for the measurement of sea surface temperatures with the NOAA polar-orbiting environmental satellites. *J. Geophys. Res.* **1998**, *103*, 27999–28012. [CrossRef]
19. Kilpatrick, K.A.; Podesta, G.P.; Evans, R. Overview of the NOAA/NASA advanced very high resolution radiometer Pathfinder algorithm for sea surface temperature and associated matchup database. *J. Geophys. Res.* **2001**, *106*, 9179–9197. [CrossRef]
20. Li, X.; Pichel, W.; Maturi, E.; Clemente-Colon, P.; Sapper, J. Deriving the operational nonlinear multichannel sea surface temperature algorithm coefficients for NOAA-15 AVHRR/3. *Int. J. Remote Sens.* **2001**, *22*, 699–704. [CrossRef]
21. May, D.A.; Osterman, W.O. Satellite-derived sea surface temperatures: Evaluation of GOES-8 and GOES-9 multispectral imager retrieval accuracy. *J. Atmos. Ocean. Technol.* **1998**, *15*, 788–797. [CrossRef]
22. Donlon, C.J.; Castro, S.L.; Kaye, A. Aircraft validation of ERS-1 ATSR and NOAA-14 AVHRR sea surface temperature measurements. *Int. J. Remote Sens.* **1999**, *20*, 3503–3513. [CrossRef]
23. Kumar, A.; Minnett, P.; Podestá, G.; Evans, R.; Kilpatrick, K. Analysis of Pathfinder SST algorithm for global and regional conditions. *J. Earth Syst. Sci.* **2000**, *109*, 395–405. [CrossRef]
24. Minnett, P.J.; Evans, R.H.; Kearns, E.J.; Brown, O.B. Sea-surface temperature measured by the Moderate Resolution Imaging Spectroradiometer (MODIS). In Proceedings of the IEEE International Geoscience and Remote Sensing Symposium (IGARSS), Toronto, ON, Canada, 24–28 June 2002.
25. Park, K.A.; Lee, E.Y.; Li, X.; Chung, S.R.; Sohn, E.H.; Hong, S. NOAA/AVHRR sea surface temperature accuracy in the East/Japan Sea. *Int. J. Digit. Earth* **2015**, *8*, 784–804. [CrossRef]
26. Hao, Y.; Cui, T.; Singh, V.P.; Zhang, J.; Yu, R.; Zhang, Z. Validation of MODIS Sea Surface Temperature Product in the Coastal Waters of the Yellow Sea. *IEEE J. Sel. Top. Appl. Earth Obs. Remote Sens.* **2017**, *10*, 1667–1680. [CrossRef]
27. Merchant, C.J.; Le Borgne, P.; Marsouin, A.; Roquet, H. Optimal estimation of sea surface temperature from split-window observations. *Remote Sens. Environ.* **2008**, *112*, 2469–2484. [CrossRef]
28. Merchant, C.J.; Harris, A.R.; Roquet, H.; Le Borgne, P. Retrieval characteristics of non-linear sea surface temperature from the Advanced Very High Resolution Radiometer. *Geophys. Res. Lett.* **2009**, *36*. [CrossRef]
29. Petrenko, B.; Ignatov, A.; Kihai, Y.; Stroup, J.; Dash, P. Evaluation and selection of SST regression algorithms for JPSS VIIRS. *J. Geophys. Res.* **2014**, *119*, 4580–4599. [CrossRef]

30. Cracknell, A.P. Remote sensing techniques in estuaries and coastal zones an update. *Int. J. Remote Sens.* **1999**, *20*, 485–496. [CrossRef]
31. Thomas, A.; Byrne, D.; Weatherbee, R. Coastal sea surface temperature variability from Landsat infrared data. *Remote Sens. Environ.* **2002**, *81*, 262–272. [CrossRef]
32. Lira, C.; Taborda, R. Advances in applied remote sensing to coastal environments using free satellite imagery. In *Remote Sensing and Modeling*; Springer: Berlin/Heidelberg, Germany, 2014; pp. 77–102.
33. Thomas, L.N.; Tandon, A.; Mahadevan, A. Submesoscale Processes and Dynamics. In *Ocean Modeling in an Eddying Regime*; American Geophysical Union: Washington, DC, USA, 2008; pp. 17–23.
34. Castro, S.; Emery, W.; Wick, G.; Tandy, W. Submesoscale sea surface temperature variability from UAV and satellite measurements. *Remote Sens.* **2017**, *9*, 1089. [CrossRef]
35. Gohin, F.; Langlois, G. Using geostatistics to merge in situ measurements and remotely-sensed observations of sea surface temperature. *Int. J. Remote Sens.* **1993**, *14*, 9–19. [CrossRef]
36. Emery, W.J.; Castro, S.; Wick, G.A.; Schluessel, P.; Donlon, C. Estimating sea surface temperature from infrared satellite and in situ temperature data. *Bull. Am. Meteorol. Soc.* **2001**, *82*, 2773–2786. [CrossRef]
37. Guinehut, S.; Le Traon, P.Y.; Larnicol, G.; Philipps, S. Combining Argo and remote-sensing data to estimate the ocean three-dimensional temperature fields A first approach based on simulated observations. *J. Mar. Syst.* **2004**, *46*, 85–98. [CrossRef]
38. Chao, Y.; Li, Z.; Farrara, J.D.; Hung, P. Blending sea surface temperatures from multiple satellites and in situ observations for coastal oceans. *J. Atmos. Ocean. Technol.* **2009**, *26*, 1415–1426. [CrossRef]
39. Banzon, V.; Smith, T.M.; Chin, T.M.; Liu, C.Y.; Hankins, W. A long-term record of blended satellite and in situ sea-surface temperature for climate monitoring, modeling and environmental studies. *Earth Syst. Sci. Data* **2016**, *8*, 165–176. [CrossRef]
40. Barron, C.N.; Kara, A.B. Satellite-based daily SSTs over the global ocean. *Geophys. Res. Lett.* **2006**, 33. [CrossRef]
41. Smit, A.J.; Roberts, M.; Anderson, R.J.; Dufois, F.; Dudley, S.F.; Bornman, T.G.; Olbers, J.; Bolton, J.J. A coastal seawater temperature dataset for biogeographical studies: Large biases between in situ and remotely-sensed data sets around the coast of South Africa. *PLoS ONE* **2013**, *8*, e81944. [CrossRef]
42. Vazquez-Cuervo, J.; Torres, H.S.; Menemenlis, D.; Chin, T.; Armstrong, E.M. Relationship between SST gradients and upwelling off Peru and Chile: Model/satellite data analysis. *Int. J. Remote Sens.* **2017**, *38*, 6599–6622. [CrossRef]
43. Ranagalage, M.; Estoque, R.C.; Murayama, Y. An urban heat island study of the Colombo metropolitan area, Sri Lanka, based on Landsat data (1997–2017). *ISPRS Int. J. Geo-Inf.* **2017**, *6*, 189. [CrossRef]
44. Roy, D.P.; Wulder, M.A.; Loveland, T.R.; Woodcock, C.E.; Allen, R.G.; Anderson, M.C.; Helder, D.; Irons, J.R.; Johnson, D.M.; Kennedy, R.; et al. Landsat-8: Science and product vision for terrestrial global change research. *Remote Sens. Environ.* **2014**, *145*, 154–172. [CrossRef]
45. Kang, K.M.; Kim, S.H.; Kim, D.J.; Cho, Y.K.; Lee, S.H. Comparison of coastal sea surface temperature derived from ship-, air-, and space-borne thermal infrared systems. In Proceedings of the IEEE International Geoscience and Remote Sensing Symposium (IGARSS), Quebec, QC, Canada, 13–18 July 2014.
46. Syariz, M.A.; Jaelani, L.M.; Subehi, L.; Pamungkas, A.; Koenhardono, E.S.; Sulisetyono, A. Retrieval of sea surface temperature over poteran island water of indonesia with Landsat 8 tirs image: A preliminary algorithm. *Remote Sens. Spat. Inf. Sci.* **2015**, *40*, 87. [CrossRef]
47. Snyder, J.; Boss, E.; Weatherbee, R.; Thomas, A.C.; Brady, D.; Newell, C. Oyster aquaculture site selection using Landsat 8-Derived Sea surface temperature, turbidity, and chlorophyll a. *Front. Mar. Sci.* **2017**, *4*, 190. [CrossRef]
48. Jiménez-Muñoz, J.C.; Sobrino, J.A.; Skoković, D.; Mattar, C.; Cristóbal, J. Land surface temperature retrieval methods from Landsat-8 thermal infrared sensor data. *IEEE Trans. Geosci. Remote Sens. Lett.* **2014**, *11*, 1840–1843. [CrossRef]
49. Rozenstein, O.; Qin, Z.; Derimian, Y.; Karnieli, A. Derivation of land surface temperature for Landsat-8 TIRS using a split window algorithm. *Sensors* **2014**, *14*, 5768–5780. [CrossRef] [PubMed]
50. Yu, X.; Guo, X.; Wu, Z. Land surface temperature retrieval from Landsat 8 TIRS—Comparison between radiative transfer equation-based method, split window algorithm and single channel method. *Remote Sens.* **2014**, *6*, 9829–9852. [CrossRef]

51. Aleskerova, A.A.; Kubryakov, A.A.; Stanichny, S.V. A two-channel method for retrieval of the Black Sea surface temperature from Landsat-8 measurements. *Izvestiya, Atmos. Ocean. Phys.* **2016**, *52*, 1155–1161. [CrossRef]
52. Bayat, F.; Hasanlou, M. Feasibility study of Landsat-8 imagery for retrieving sea surface temperature (case study Persian Gulf). *Remote Sens. Spat. Inf. Sci.* **2016**, *41*. [CrossRef]
53. Cahyono, A.B.; Saptarini, D.; Pribadi, C.B.; Armono, H.D. Estimation of sea surface temperature (SST) using split window methods for monitoring industrial activity in coastal area. *Appl. Mech. Mater.* **2017**, *862*, 90–95. [CrossRef]
54. Jaelani, L.M.; Alfatinah, A. Sea surface temperature mapping at medium scale using Landsat 8-TIRS satellite image. *IPTEK J. Proc. Ser.* **2017**, *3*, 582–586. [CrossRef]
55. Xufeng, X.; Yang, L.; Wentong, D.; Zhonglin, W.; Lianlong, Z.; Zhen, S.; Miaofen, H. An algorithm to Inverse Sea Surface Temperatures at Offshore. Available online: http://citeseer.ist.psu.edu/viewdoc/download;jsessionid=2E38FC329B20BDD8666007C82EDA06A3?doi=10.1.1.741.7959&rep=rep1&type=pdf (accessed on 19 September 2019).
56. Park, K.A.; Chung, J.Y.; Kim, K.; Cornillon, P.C. Wind and bathymetric forcing of the annual sea surface temperature signal in the East (Japan) Sea. *Geophys. Res. Lett.* **2005**, *32*. [CrossRef]
57. Park, K.A.; Lee, E.Y.; Chang, E.; Hong, S. Spatial and temporal variability of sea surface temperature and warming trends in the Yellow Sea. *J. Mar. Syst.* **2015**, *143*, 24–38. [CrossRef]
58. Park, K.A.; Park, J.J.; Park, J.E.; Choi, B.J.; Lee, S.H.; Byun, D.S.; Lee, E.I.; Kang, B.S.; Shin, H.R.; Lee, S.R. *Interdisciplinary Mathematics and Sciences in Schematic Ocean Current Maps in the Seas Around Korea. Handbook of the Mathematics of the Arts and Sciences*; Springer: Berlin/Heidelberg, Germany, 2019.
59. Hosoda, K.; Murakami, H.; Sakaida, F.; Kawamura, H. Algorithm and validation of sea surface temperature observation using MODIS sensors aboard Terra and Aqua in the western North Pacific. *J. Oceanogr.* **2007**, *63*, 267–280. [CrossRef]
60. Stark, J.D.; Donlon, C.J.; Martin, M.J.; McCulloch, M.E. OSTIA: An operational, high resolution, real time, global sea surface temperature analysis system. In Proceedings of the IEEE Oceans, Aberdeen, UK, 18–21 June 2007.
61. Donlon, C.; Robinson, I.; Casey, K.S.; Vazquez-Cuervo, J.; Armstrong, E.; Arino, O.; Gentemann, C.; May, D.; LeBorgne, P.; Piollé, J.; et al. The global ocean data assimilation experiment high-resolution sea surface temperature pilot project. *Bull. Am. Meteorol. Soc.* **2007**, *88*, 1197–1213. [CrossRef]
62. Martin, M.J.; Hines, A.; Bell, M.J. Data assimilation in the FOAM operational short-range ocean forecasting system: A description of the scheme and its impact. *Q. J. R. Meteorol. Soc.* **2007**, *133*, 981–995. [CrossRef]
63. Irish, R.R.; Barker, J.L.; Goward, S.N.; Arvidson, T. Characterization of the Landsat-7 ETM+ automated cloud-cover assessment (ACCA) algorithm. *Photogramm. Eng. Remote Sens.* **2006**, *72*, 1179–1188. [CrossRef]
64. Roy, D.P.; Ju, J.; Kline, K.; Scaramuzza, P.L.; Kovalskyy, V.; Hansen, M.; Loveland, T.R.; Vermote, E.; Zhang, C. Web-enabled Landsat Data (WELD): Landsat ETM+ composited mosaics of the conterminous United States. *Remote Sens. Environ.* **2010**, *114*, 35–49. [CrossRef]
65. Zhu, Z.; Woodcock, C.E. Object-based cloud and cloud shadow detection in Landsat imagery. *Remote Sens. Environ.* **2012**, *118*, 83–94. [CrossRef]
66. Oreopoulos, L.; Wilson, M.J.; Várnai, T. Implementation on Landsat data of a simple cloud-mask algorithm developed for MODIS land bands. *IEEE Trans. Geosci. Remote Sens. Lett.* **2011**, *8*, 597–601. [CrossRef]
67. Wilson, M.J.; Oreopoulos, L. Enhancing a simple MODIS CLOUD mask algorithm for the Landsat data continuity mission. *IEEE Trans. Geosci. Remote Sens.* **2013**, *51*, 723–731. [CrossRef]
68. Zhu, Z.; Wang, S.; Woodcock, C.E. Improvement and expansion of the Fmask algorithm: Cloud, cloud shadow, and snow detection for Landsats 4–7, 8, and Sentinel 2 images. *Remote Sens. Environ.* **2015**, *159*, 269–277. [CrossRef]
69. Luo, Y.; Trishchenko, A.P.; Khlopenkov, K.V. Developing clearsky, cloud, and cloud shadow mask for producing clear-sky composites at 250-meter spatial resolution for the seven MODIS land bands over Canada and North America. *Remote Sens. Environ.* **2008**, *112*, 4167–4185. [CrossRef]
70. Inoue, T. A cloud type classification with NOAA 7 split-window measurements. *J. Geophys. Res.* **1987**, *92*, 3991–4000. [CrossRef]
71. Gao, B.C.; Kaufman, Y.J. Selection of the 1.375-um MODIS channel for remote sensing of cirrus clouds and stratospheric aerosols from space. *J. Atmos. Sci.* **1995**, *52*, 4231–4237. [CrossRef]

72. Petrenko, B.; Ignatov, A.; Kihai, Y.; Heidinger, A. Clear-sky mask for the advanced clear-sky processor for oceans. *J. Atmos. Ocean. Technol.* **2010**, *27*, 1609–1623. [CrossRef]
73. Cayula, J.F.P.; May, D.A.; McKenzie, B.D.; Willis, K.D. VIIRS-derived SST at the Naval Oceanographic Office: From evaluation to operation. In Proceedings of the SPIE, Baltimore, MD, USA, 29 April–3 May 2013; Volume 8724.
74. McBride, W.; Arnone, R.; Cayula, J.F. Improvements of satellite SST retrievals at full swath. In Proceedings of the SPIE, Baltimore, MD, USA, 29 April–3 May 2013; Volume 8724.
75. Marsouin, A.; Le Borgne, P.; Legendre, G.; Péré, S.; Roquet, H. Six years of OSI-SAF METOP-A AVHRR sea surface temperature. *Remote Sens. Environ.* **2015**, *159*, 288–306. [CrossRef]
76. Li, F.; Jupp, D.L.; Reddy, S.; Lymburner, L.; Mueller, N.; Tan, P.; Islam, A. An evaluation of the use of atmospheric and BRDF correction to standardize Landsat data. *IEEE J. Sel. Top. Appl. Earth Obs. Remote Sens.* **2010**, *3*, 257–270. [CrossRef]
77. Trezza, R.; Allen, R.; Tasumi, M. Estimation of actual evapotranspiration along the Middle Rio Grande of New Mexico using MODIS and landsat imagery with the METRIC model. *Remote Sens.* **2013**, *5*, 5397–5423. [CrossRef]
78. Gao, F.; Hilker, T.; Zhu, X.; Anderson, M.; Masek, J.; Wang, P.; Yang, Y. Fusing Landsat and MODIS data for vegetation monitoring. *IEEE Geosci. Remote Sens. Mag.* **2015**, *3*, 47–60. [CrossRef]
79. Roy, D.P.; Zhang, H.K.; Ju, J.; Gomez-Dans, J.L.; Lewis, P.E.; Schaaf, C.B.; Sun, Q.; Li, J.; Huang, H.; Kovalskyy, V. A general method to normalize Landsat reflectance data to nadir BRDF adjusted reflectance. *Remote Sens. Environ.* **2016**, *176*, 255–271. [CrossRef]
80. Du, C.; Ren, H.; Qin, Q.; Meng, J.; Zhao, S. A practical split-window algorithm for estimating land surface temperature from Landsat 8 data. *Remote Sens.* **2015**, *7*, 647–665. [CrossRef]
81. Robinson, I.S. *Measuring the Ocean from Space—The Principles and Methods of Satellite Oceanography*; Springer: Berlin/Heidelberg, Germany, 2004.
82. Xu, F.; Ignatov, A. In situ SST Quality Monitor (iQUAM). *J. Atmos. Ocean. Technol.* **2014**, *31*, 164–180. [CrossRef]
83. Woo, H.J.; Park, K.; Li, X.; Lee, E.Y. Sea Surface Temperature Retrieval from the First Korean Geostationary Satellite COMS Data: Validation and Error Assessment. *Remote Sens.* **2018**, *10*, 1916. [CrossRef]
84. Hosoda, K.; Sakaida, F. Global Daily High-Resolution Satellite-Based Foundation Sea Surface Temperature Dataset: Development and Validation against Two Definitions of Foundation SST. *Remote Sens.* **2016**, *8*, 962. [CrossRef]
85. Alsweiss, S.O.; Jelenak, Z.; Chang, P.S. Remote Sensing of Sea Surface Temperature Using AMSR-2 Measurements. *IEEE J. Sel. Top. Appl. Earth Obs. Remote Sens.* **2017**, *10*, 3948–3954. [CrossRef]
86. Kumar, A.; Minnett, P.J.; Podestá, G.; Evans, R.H. Error characteristics of the atmospheric correction algorithms used in retrieval of sea surface temperatures from infrared satellite measurements: Global and regional aspects. *J. Atmos. Sci.* **2003**, *60*, 575–585. [CrossRef]
87. Barton, I.J. Satellite-derived sea surface temperatures-A comparison between operational, theoretical, and experimental algorithms. *J. Appl. Meteorol.* **1992**, *31*, 433–442. [CrossRef]
88. Donlon, C.J.; Robinson, I.S. Observations of the oceanic thermal skin in the Atlantic Ocean. *J. Geophys. Res.* **1997**, *102*, 18585–18606. [CrossRef]
89. Donlon, C.J.; Nightingale, T.J.; Sheasby, T.; Turner, J.; Robinson, I.S.; Emergy, W.J. Implications of the oceanic thermal skin temperature deviation at high wind speed. *Geophys. Res. Lett.* **1999**, *26*, 2505–2508. [CrossRef]
90. Murray, M.J.; Allen, M.R.; Merchant, C.J.; Harris, A.R.; Donlon, C.J. Direct observations of skin-bulk SST variability. *Geophys. Res. Lett.* **2000**, *27*, 1171–1174. [CrossRef]
91. Barton, I.J. Interpretation of satellite-derived sea surface temperatures. *Adv. Space Res.* **2001**, *28*, 165–170. [CrossRef]
92. Minnett, P.J. Radiometric measurements of the sea-surface skin temperature: The competing roles of the diurnal thermocline and the cool skin. *Int. J. Remote Sens.* **2003**, *24*, 5033–5047. [CrossRef]
93. Oesch, D.C.; Jaquet, J.M.; Hauser, A.; Wunderle, S. Lake surface water temperature retrieval using advanced very high resolution radiometer and Moderate Resolution Imaging Spectroradiometer data: Validation and feasibility study. *J. Geophys. Res.* **2005**, 110. [CrossRef]
94. Kawai, Y.; Wada, A. Diurnal sea surface temperature variation and its impact on the atmosphere and ocean: A review. *J. Oceanogr.* **2007**, *63*, 721–744. [CrossRef]

95. Donlon, C.J.; Eifler, W.; Nightingale, T.J. The thermal skin temperature of the ocean at high wind speed. In Proceedings of the IEEE International Geoscience and Remote Sensing Symposium (IGARSS), Hamburg, Germany, 28 June–2 July 1999.
96. Qiu, C.; Wang, D.; Kawamura, H.; Guan, L.; Qin, H. Validation of AVHRR and TMI-derived sea surface temperature in the northern South China Sea. *Cont. Shelf Res.* **2009**, *29*, 2358–2366. [CrossRef]